



## Article

# A Miniature Flapping Mechanism Using an Origami-Based Spherical Six-Bar Pattern

Seung-Yong Bae <sup>1</sup>, Je-Sung Koh <sup>2</sup>  and Gwang-Pil Jung <sup>1,\*</sup> 

<sup>1</sup> Department of Mechanical and Automotive Engineering, Seoul National University of Science and Technology, Seoul 01811, Korea; qo1113@seoultech.ac.kr

<sup>2</sup> Department of Mechanical Engineering, Ajou University, Suwon-si 16499, Korea; jskoh@ajou.ac.kr

\* Correspondence: gpjung@seoultech.ac.kr

**Abstract:** In this paper, we suggest a novel transmission for the DC motor-based flapping-wing micro aerial vehicles (FWMAVs). Most DC motor-based FWMAVs employ linkage structures, such as a crank-rocker or a crank-slider, which are designed to transmit the motor's rotating motion to the wing's flapping motion. These transmitting linkages have shown successful performance; however, they entail the possibility of mechanical wear originating from the friction between relative moving components and require an onerous assembly process owing to several tiny components. To reduce the assembly process and wear problems, we present a geometrically constrained and origami-based spherical six-bar linkage. The origami-based fabrication method reduces the number of the relative moving components by replacing rigid links and pin joints with facets and folding joints, which shortens the assembly process and reduces friction between components. The constrained spherical six-bar linkage enables us to change the motor's rotating motion to the linear reciprocating motion. Due to the property that every axis passes through a single central point, the motor's rotating motion is filtered at the spherical linkage and does not transfer to the flapping wing. Only linear motion, therefore, is passed to the flapping wing. To show the feasibility of the idea, a prototype is fabricated and analyzed by measuring the flapping angle, the wing rotation angle and the thrust.



**Citation:** Bae, S.-Y.; Koh, J.-S.; Jung, G.-P. A Miniature Flapping Mechanism Using an Origami-Based Spherical Six-Bar Pattern. *Appl. Sci.* **2021**, *11*, 1515. <https://doi.org/10.3390/app11041515>

Academic Editor: Nicola Pio Belfiore  
Received: 22 December 2020  
Accepted: 3 February 2021  
Published: 8 February 2021

**Publisher's Note:** MDPI stays neutral with regard to jurisdictional claims in published maps and institutional affiliations.



**Copyright:** © 2021 by the authors. Licensee MDPI, Basel, Switzerland. This article is an open access article distributed under the terms and conditions of the Creative Commons Attribution (CC BY) license (<https://creativecommons.org/licenses/by/4.0/>).

**Keywords:** bio-inspired robot; micro aerial vehicle; flapping mechanism

## 1. Introduction

Flapping-wing micro air vehicles (FWMAVs) have been widely studied due to their agility and maneuverability in the air. These properties can be applied to the areas of reconnaissance for military and exploration missions for disaster areas. For example, they can easily approach tiny cracks at disaster areas or enemy camps without being recognized.

To enable successful working of FWMAVs, researchers have employed a variety of actuators such as DC motors [1–19], piezoelectric actuators [20–23], electromagnetic actuators [24–28], and electrostatic actuators [6,29].

Among these actuators, in this paper, we suggest a novel transmission mechanism to reduce the assembly process and wear problems for the DC motor-based FWMAVs. In the case of DC motor-based FWMAVs, most of them use linkage structures to transmit the motor's rotating motion to the wing's flapping motion. These transmitting linkages have involve the possibility of mechanical wear originating from the friction between relative moving components and requires an onerous assembly process owing to several tiny components. Types of the transmissions used for the DC motor-based FWMAVs are given in Table 1.

Previously, a variety of transmission mechanisms have been employed. Galinski et al. used a spatial mechanism based on the double Scotch yoke [15]. They proposed to use spherical type of double Scotch yoke to overcome drawbacks of the planar Scotch yoke. Oppenheimer et al. and Sahai et al. employed four-bar linkages to change the motor's rotating motion to the flapping motion [5,12]. Karasek et al. and Wagter et al. also made

flapping mechanisms using crank-rocker four-bar linkages [2,4]. Takahashi et al. and Lau et al. made flapping mechanisms using crank-sliders [1,9]. The sliders enabled the mechanism to have reciprocating motion of the wings. Ristroph et al. and Gaissert et al. applied crank-shaft mechanisms [8,11]. The crank-shaft mechanisms converted motors' rotating movement into an oscillating movement of the wings. Roshanbin et al. proposed a flapping robot, COLIBRI, by combining four-bar linkage and a slider-crank mechanism [16].

**Table 1.** Transmission mechanisms used for DC motor-based flapping-wing micro air vehicles (FWMAVs).

Mechanism Types	Possibility of Mechanical Wear	Difficulty of Assembly	Transmission Efficiency
Scotch-yoke [15]	Yes	Dexterity is required	High (rotating in one direction)
Crank-rocker [2,4,5,12]	Yes	Dexterity is required	High (rotating in one direction)
Crank-slider [1,8,9,11,16]	Yes	Dexterity is required	High (rotating in one direction)
String-based [3,7,13,17–19]	No	Dexterity is required	High (rotating in one direction)
Proposed mechanism	No	Easy	High (rotating in one direction)
Direct drive [10,14]	No	Easy	Low (vibrate back and forth)

To reduce the mass and complexity of the transmission structures, some researchers suggested a string-based flapping mechanism or direct-driven mechanisms [7]. Keennon et al. and Gong et al. used string-based flapping mechanisms [3,13]. KUbeetle [17–19] mixed four-bar linkages and a string-based pulley mechanism. The string-based transmission enabled the prevention of mechanical wear and fracture of moving parts. The direct-driven mechanisms enabled the extreme reduction in the mechanical structures for transmission [10,14]. The direct-driven mechanisms achieved a high lift-to-weight ratio by resonating the system.

In this paper, we suggest a novel transmission mechanism to reduce the assembly process and wear problems for the DC motor-based FWMAVs. To make this possible, two design approaches have been utilized: origami-based fabrication and geometrically constrained spherical six-bar linkage. The origami-based fabrication method reduces the number of relative moving components by replacing rigid links and pin joints with facets and folding joints, which shortens the assembly process and reduces wear problems [30,31]. The geometrically constrained spherical six-bar linkage enables the change in the motor's rotating motion to the linear reciprocating motion. Due to the property that every axis passes through a single central point, the constrained spherical six-bar linkage filters the rotating motion of the DC motor and passes only linear motion to the flapping wings. Using the proposed design approaches, a novel flapping mechanism is made as shown in Figure 1.

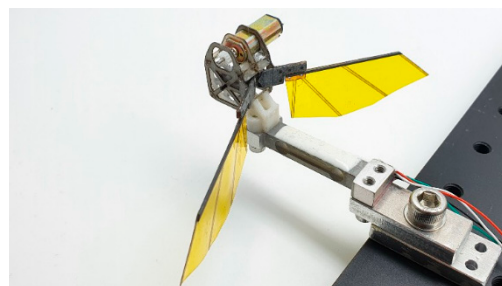


**Figure 1.** The developed prototype FWMAV based on flapping mechanism using a constrained spherical six-bar linkage.

This paper is organized as follows: The design section describes the concept of the flapping mechanism and the working process of the origami-based constrained spherical six-bar. To precisely investigate the mechanism and to select the proper geometric parameters, a three-dimensional kinematic model has been made. Furthermore, an experiment has been conducted to check the feasibility of the developed flapping mechanism by measuring the flapping frequency, angle, wing rotation angle and thrust.

## 2. Design

The overall design is shown in Figure 1. A DC motor is located at the top of the mechanism and the shaft is connected to the spur gear. The spur gear plays a role as a crank. The connecting rod connects the crank and the spherical six-bar linkage. The spherical six-bar linkage transmits the motor's motion to the flapping wing.

### 2.1. Flapping Mechanism

One important point is that only linear motion should be transmitted to generate the flapping motion of the wings. To make this possible, one end of the spherical six-bar linkage is fixed at the body frame as shown in Figure 2g. This constraint filters the rotating motion of the motor and transmits the linearly reciprocating motion only, which is shown in Video S1. By using this working principle, a successful flapping motion can be achieved without mechanical parts that cause friction problems.

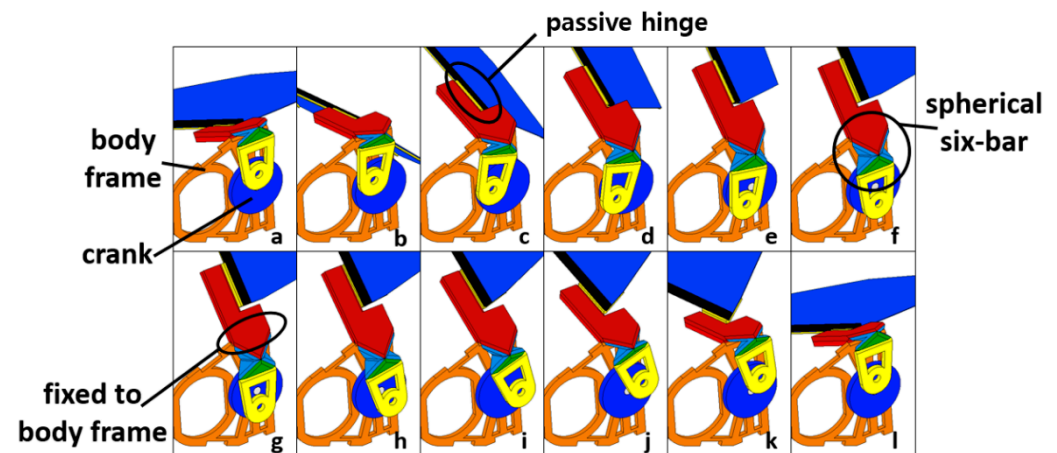


Figure 2. Snapshots of the moving process of the transmission. From (a–f), the mechanism shows upstroke. From (g–l), downstroke is shown.

To generate the thrust in the end, a wing rotating motion is necessarily required. To achieve the wing rotating motion, passive hinges are employed as shown in Figure 2c. The passive joints are positioned between the output of the transmission and the wings. The passive hinges are parallel to the spanwise direction and have a joint-stop to prevent excessive rotation. Overall, the system has three degrees of freedom—flapping actuation and two passive hinges for wing rotation.

Flapping motion is achieved by the constrained spherical six-bar linkage shown in Figure 3, which is the key enabling technology of the proposed mechanism. Generally, the spherical six-bar linkage has complex structures due to many joints, links, and axes. The spherical six-bar linkage shown in Figure 2 is designed using an origami-based pattern and fabricated through a layer-based method: smart composite microstructures (SCM). This process provides lightweight structures by replacing pin joints with flexures and finally enables us to achieve spherical six-bar linkage by folding a paper just three times.

Figure 3 shows the pattern for the origami-based spherical six-bar linkage. All axes of the flexures pass through a single point and rotate around the point. The spherical six-bar array is installed between the wing and the crank as shown in Figure 2. The spherical linkage acts as a mechanical filter, which transmits only linear motion to the wings. This

is possible since one end of the linkage is constrained. The motor and the cranks make the rotating motion. When this rotating motion passes through the spherical linkage, the horizontal motion is absorbed by the spherical linkage but the vertical motion is transmitted to the wing.

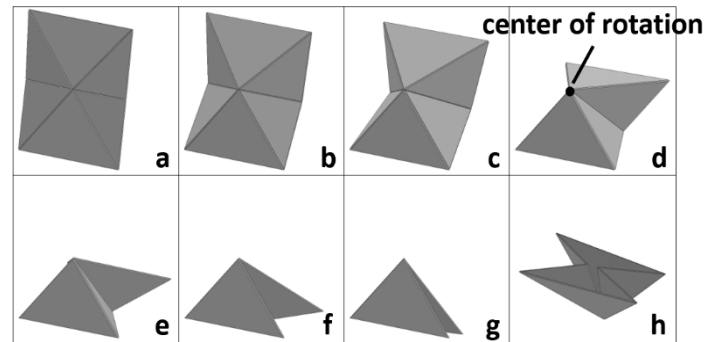


**Figure 3.** Snapshots of the origami-based spherical six-bar linkage. All axes of the flexure joints (folding line) pass through the rotation center indicated in (d). The pattern is folded from (a–g). The backside of the pattern is shown in (h).

Depending on how we choose to constrain the direction of the axis, the direction of the output motion can be differed. In our case, we need a flapping motion vertical to the motor’s axis. Therefore, the axis constrained has been determined as a direction perpendicular to the span wise direction, which is equal to the direction of the motor’s axis. Figure 2 shows how the constrained spherical six-bar works.

2.2. Fabrication

The proposed mechanism has been designed to have wingspan of 125 mm, which is referred to as the size of a beetle [32,33]. The beetle has appropriate size and mass, considering our fabrication capacity—the machining resolution is about 500 μm and this resolution is not enough to make micro-scale flappers. The body has the size of 20 mm × 10 mm × 10 mm and the whole mechanism weighs 5.7 g. Its planar design is shown in Figure 4B, which consist of twenty joints and eighteen links. To manufacture and assemble these tiny and complex kinematic structures using conventional pins and links needs much effort and the structure tends to be heavy because of the increased number of components.

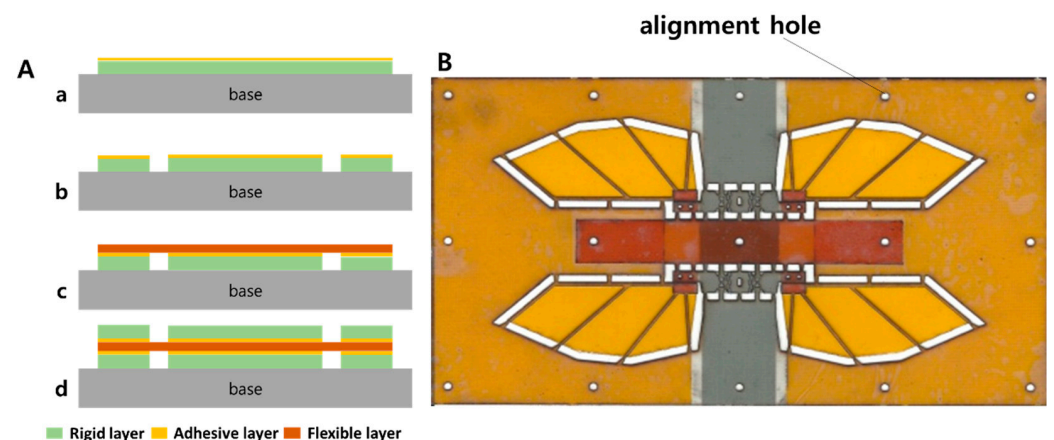


**Figure 4.** (A) The process of smart composite microstructures (SCM). The rigid layer with the adhesive is prepared (a). The joints are selectively cut by the laser machine (b). The flexible layer (rip-stop fabric) is sandwiched between two rigid layers (c,d). (B) The manufactured flapping mechanism before assembly. The mechanism is assembled by folding the flexible joints.

To avoid these issues, the SCM process is applied [30]. The SCM process replaces the conventional pin joints and links with the flexure joints and composite links. In Figure 4, the whole fabrication process is shown and described. For the proposed mechanism, a glass fiber board (200  $\mu\text{m}$  thickness) is used as the rigid links and the rip-stop fabric (200  $\mu\text{m}$  thickness) is employed as the flexure joints. The flapping wings are also designed to be manufactured through the SCM process with the body frame. The wing has the size of 50 mm  $\times$  20 mm and includes glass fiber supporters to prevent unwanted bending induced by air resistance during flapping, which is shown in Figure 4B. For the wing membrane, 25  $\mu\text{m}$  polyimide film has been applied. Due to the SCM process, the whole mechanism weighs 5.7 g and the mass budget is shown in Table 2.

Table 2. Mass Budget.

Components	Quantity (ea.)	Mass (g)	Ratio to Overall Mass (%)
Flapping wing	2	0.12	4.21
Motor	1	3.9	68.42
Transmission	2	0.24	8.42
Body frame	1	1.08	18.95
Total	-	5.7	100.0

### 3. Mechanism Analysis

Kinematic modeling is done to determine lengths of links and accordingly get the desired performance—stable flapping posture and high thrust. To achieve the desired performance, two conditions must be satisfied. First, the flapping angle output should be symmetric to prevent pitch torque. Second, in order to maintain the angle of attack (AoA) and gain sufficient momentum, the upstroke and downstroke speed need to be as equal as possible. If the above two conditions are satisfied, the relation between the input crank angle and the output flapping angle has an ideal cosine curve as shown in Figure 5. In Figure 5, an optimized case and an arbitrary case are given. To satisfy the two required conditions, the flapping mechanism needs to be designed so that the flapping angle curve passes through the point *a*, *b*, *c* and *d*. To investigate the geometrical requirement to fulfill the conditions, kinematic modeling and analysis have been done.

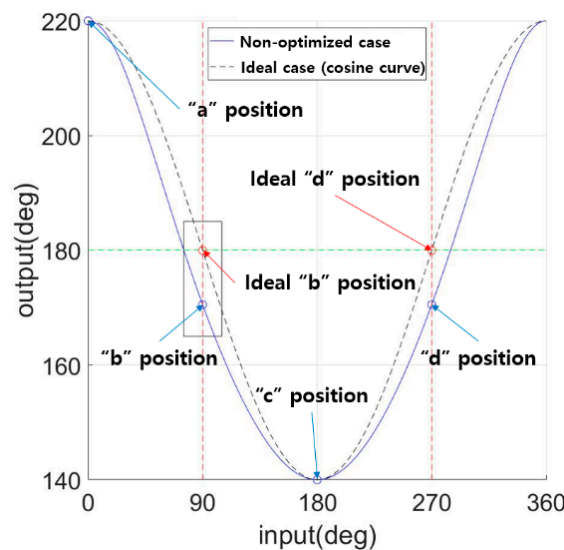


Figure 5. The secondary condition. A non-optimized case and an ideal case are simultaneously shown to compare the difference.



### 3.1. Kinematic Modeling

For three-dimensional analysis, the spherical coordinate system is employed as shown in Figure 6. Based on the coordinate, a vector loop formula is derived as follows:

$$\vec{r} + \vec{L}_3 + \vec{L}_2 + \vec{L}_1 = \vec{G} \tag{1}$$

$$r \begin{bmatrix} \cos \theta_1 \\ \sin \theta_1 \\ 0 \end{bmatrix} + L_3 \begin{bmatrix} \cos \theta_2 \\ \sin \theta_2 \\ 0 \end{bmatrix} + L_2 \begin{bmatrix} \sin \phi_3 \cos \theta_2 \\ \sin \phi_3 \sin \theta_2 \\ \cos \phi_3 \end{bmatrix} + L_1 \begin{bmatrix} \sin \phi_4 \\ 0 \\ \cos \phi_4 \end{bmatrix} = \begin{bmatrix} G \\ 0 \\ -d \end{bmatrix} \tag{2}$$

where  $r, L_1, L_2$  and  $L_3$  are the length of the crank, the output link, the connecting rod, and the spherical bar, respectively. The angle parameters such as  $\theta_1, \phi_4, \theta_2,$  and  $\phi_3$  are indicated in Figure 6.

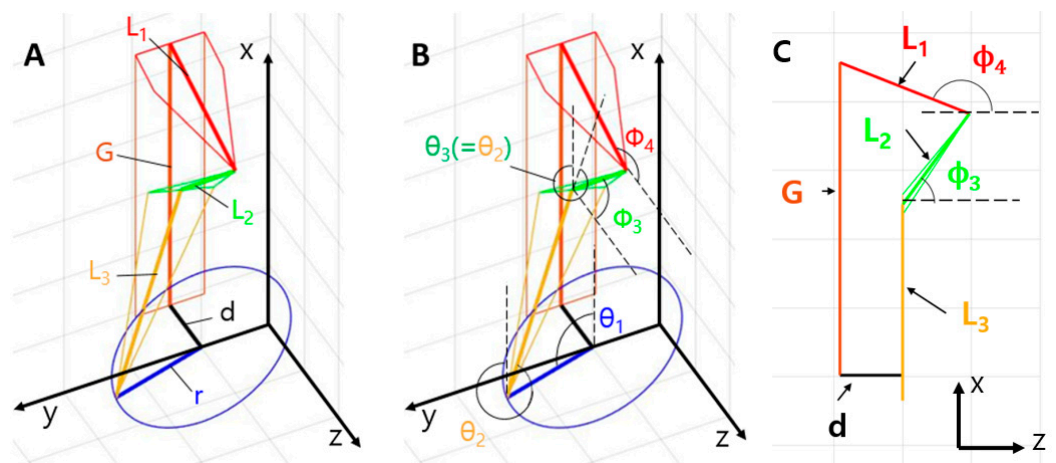


**Figure 6.** The vector loop of the constrained spherical six-bar transmission for the kinematic analysis. Diagonal view (A,B) and x-z plane view (C).

For the first condition, the transmission needs to be designed for the wings to have a symmetric flapping angle,  $\pm 40^\circ$ , from the neutral position. When applied to this kinematic modeling, the highest and lowest values of  $\phi_4$  based on the neutral point ( $\phi_4 = 180^\circ$ ) are generated as  $180^\circ + 40^\circ$  and  $180^\circ - 40^\circ$ , respectively.

$$r \begin{bmatrix} 1 \\ 0 \\ 0 \end{bmatrix} + L_3 \begin{bmatrix} 1 \\ 0 \\ 0 \end{bmatrix} + L_2 \begin{bmatrix} \sin \phi_3 \\ 0 \\ \cos \phi_3 \end{bmatrix} + L_1 \begin{bmatrix} \sin(180^\circ + 40^\circ) \\ 0 \\ \cos(180^\circ + 40^\circ) \end{bmatrix} = \begin{bmatrix} G \\ 0 \\ -d \end{bmatrix} \tag{3}$$

$$\begin{bmatrix} -1 \\ 0 \\ 0 \end{bmatrix} + L_3 \begin{bmatrix} 1 \\ 0 \\ 0 \end{bmatrix} + L_2 \begin{bmatrix} \sin \phi_3 \\ 0 \\ \cos \phi_3 \end{bmatrix} + L_1 \begin{bmatrix} \sin(180^\circ - 40^\circ) \\ 0 \\ \cos(180^\circ - 40^\circ) \end{bmatrix} = \begin{bmatrix} G \\ 0 \\ -d \end{bmatrix} \tag{4}$$

Based on the Equations (3) and (4), the relation between  $L_2$  and  $L_3$  is given as follows:

$$L_2^2 = (G - L_3)^2 + \left( \frac{r}{\tan 40^\circ} - d \right)^2 \tag{5}$$

The secondary condition is to make the neutral of the crank and the neutral of the wing equal. In order to get the thrust during a wing-beat cycle, the key is to maintain the angle of attack (AoA) of the wing. Theoretically, when the equal shape and speed of the wings are given,  $45^\circ$  is the proper AoA for the maximum thrust [34].

In order to maintain the AoA, the wing angular velocities of upstroke and downstroke need to be as symmetrical and constant as possible. This condition is indicated in Figure 6, which shows the relation between the flapping angle and the crank angle. When the curve

corresponds to the ideal cosine curve, the condition is satisfied. In Figure 6, the output flapping angle is  $\pi$  when the crank input angle is  $\pi/2$  and  $3\pi/2$ . That is, it is preferable that the path length is the same as the path length between the highest point and the neutral point (from the point  $a$  and  $b$ ) and the path length between the neutral point and the lowest point (from the point  $b$  to  $c$ ).

$$r \begin{bmatrix} 0 \\ 1 \\ 0 \end{bmatrix} + L_3 \begin{bmatrix} \cos \theta_{2b} \\ \sin \theta_{2b} \\ 0 \end{bmatrix} + L_2 \begin{bmatrix} \sin \phi_{3b} \cos \theta_{2b} \\ \sin \phi_{3b} \sin \theta_{2b} \\ \cos \phi_{3b} \end{bmatrix} + L_1 \begin{bmatrix} 0 \\ 0 \\ -1 \end{bmatrix} = \begin{bmatrix} G \\ 0 \\ -d \end{bmatrix} \quad (6)$$

$$r \begin{bmatrix} 0 \\ -1 \\ 0 \end{bmatrix} + L_3 \begin{bmatrix} \cos \theta_{2d} \\ \sin \theta_{2d} \\ 0 \end{bmatrix} + L_2 \begin{bmatrix} \sin \phi_{3d} \cos \theta_{2d} \\ \sin \phi_{3d} \sin \theta_{2d} \\ \cos \phi_{3d} \end{bmatrix} + L_1 \begin{bmatrix} 0 \\ 0 \\ -1 \end{bmatrix} = \begin{bmatrix} G \\ 0 \\ -d \end{bmatrix} \quad (7)$$

where  $\phi_{3b} = \phi_{3d}$ ,  $\theta_{2b} + \theta_{2d} = 2\pi$ .  $\theta_{2b}$  and  $\theta_{2d}$  are when  $\theta_2$  is in point  $b$  and  $d$ , respectively, as shown in Figure 6.

Based on the Equations (6) or (7), the relation between  $L_2$  and  $L_3$  is given as follows:

$$(L_3 + L_2 \sin \phi_{3b \text{ or } 3d})^2 = G^2 + r^2 \quad (8)$$

$$L_2 \cos \phi_{3b \text{ or } 3d} - L_1 = -d \quad (9)$$

The term,  $\cos \phi_{3b \text{ or } 3d}$ , is eliminated from the Equations (8) and (9). In result, following equation is given:

$$L_2 = \sqrt{(\sqrt{G^2 + r^2} - L_3)^2 + (L_1 - d)^2} \quad (10)$$

By using the two conditions—Equations (5) and (10)—optimized geometrical values can be determined.

### 3.2. Parameter Selection

Considering the whole size of the flapping mechanism,  $L_1$ ,  $G$ ,  $d$  and  $r$  are initially determined as 10.11 mm, 22.75 mm, 4.5 mm, and 6.5 mm, respectively. Figure 7a shows the change in the output flapping angle according to the length ratio of  $L_2$  and  $L_3$  to the crank length  $r$ .

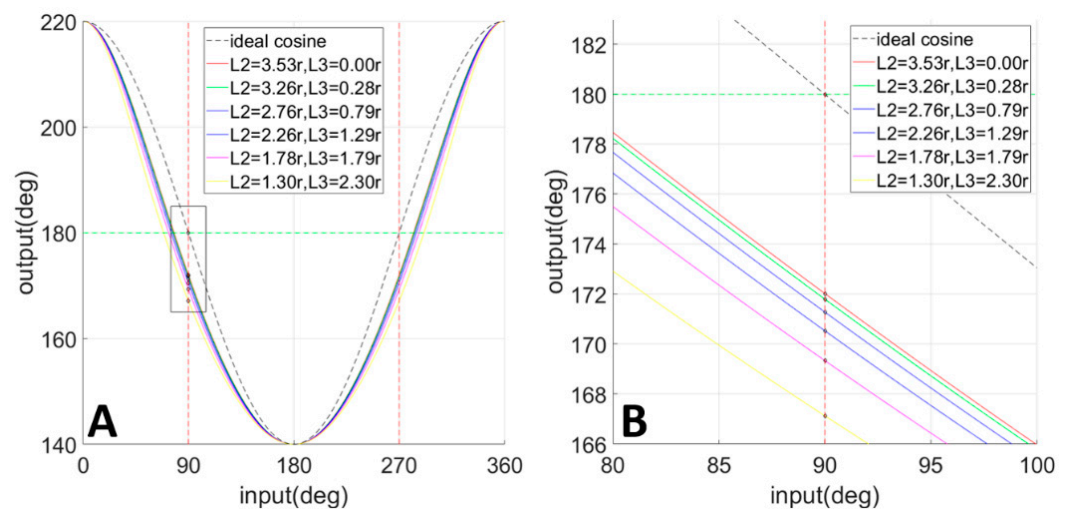


**Figure 7.** (A) Simulated output flapping angle vs. input crank angle by varying  $L_2$  and  $L_3$ . (B) The magnification of the rectangle indicated in (A).

In Figure 7b, as  $L_2$  increases and  $L_3$  decreases, the curve becomes similar to the ideal cosine. The case when  $L_2$  is 3.53  $r$  and  $L_3$  is 0.00  $r$  is the closest one. However, it is difficult

to make a certain link length zero because of realistic problems such as material thickness, or inter-part interference. Therefore,  $L_2$  and  $L_3$  are determined as 8.38 mm (=1.30 r) and 14.72 mm (=2.30 r), respectively, which correspond to the yellow line in Figure 7.

#### 4. Experimental Results

To check whether the proposed transmission and the flapping mechanism properly works or not, experimental tests have been done. By using the high-speed camera, the flapping angle, frequency, and wing rotation angle are observed. In addition, the thrust is measured using a load cell to investigate the performance of the flapping mechanism.

##### 4.1. Flapping Mechanism

Figures 8 and 9 show the snapshots during flapping. The snapshots are taken by a high-speed camera with the frame rate of 900. To investigate the flapping angle and the wing rotation angle, the mechanism is filmed from the top and side. To operate the flapping mechanism, 3.8 V and 580 mA are given to the DC motor. Based on the Figures 8 and 9 the mechanism operates with the flapping frequency of 23 Hz.

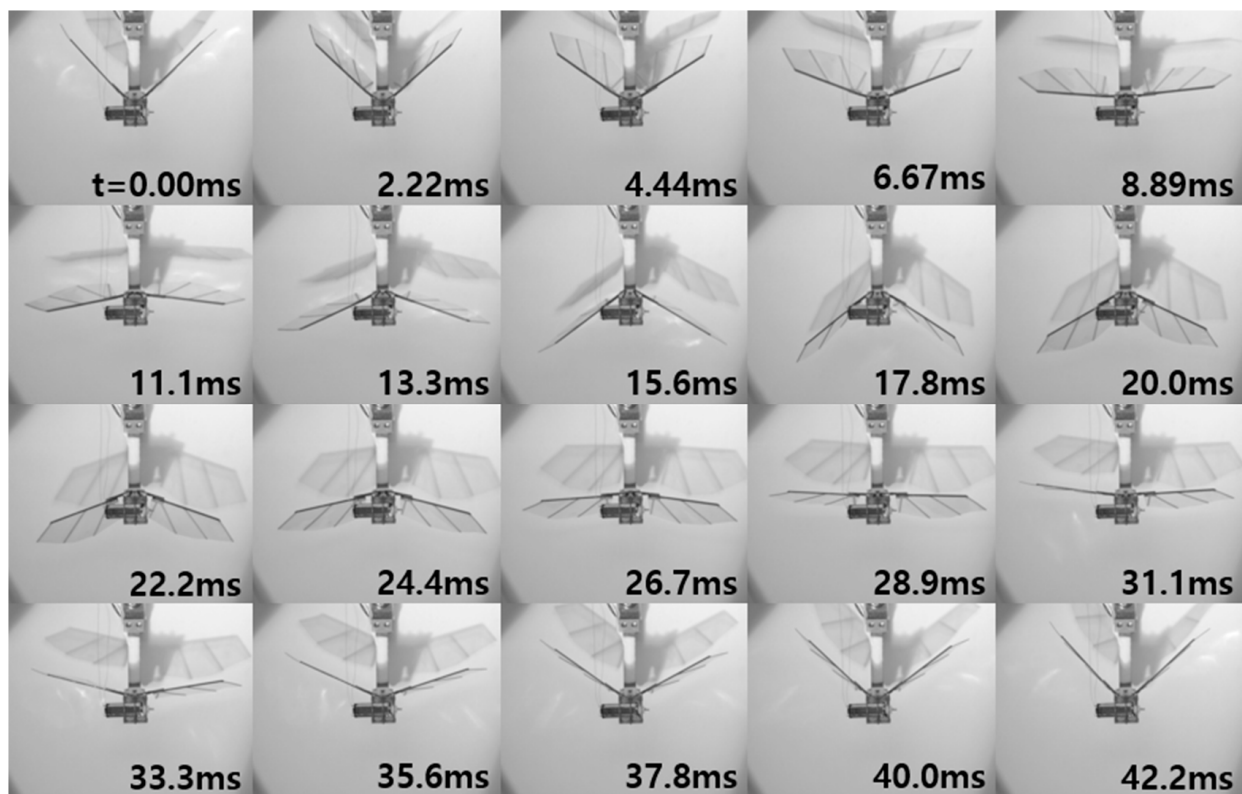


**Figure 8.** Snapshots while flapping at 23 Hz. A high-speed video of flapping, taken at 900 fps. Flapping angle can be measured from the top view.

The flapping angle is shown in Figure 8. For the right wing, the flapping angles are measured as  $+42^\circ$  and  $-37^\circ$  with respect to the neutral point;  $50^\circ$  and  $-36.5^\circ$  are measured in case of the left wing. This result is confirmed through Figure 10. Figure 10 shows the flapping angles depending on the crank angle. The left wing has flapping angle range of  $86.5^\circ$  ( $141.5^\circ \sim 228^\circ$ ) and the right wing has  $77^\circ$  ( $144^\circ \sim 223^\circ$ ). There exists a  $10^\circ$  difference between two wings. The difference may occur due to the problems coming from fabrication and assembly issues.



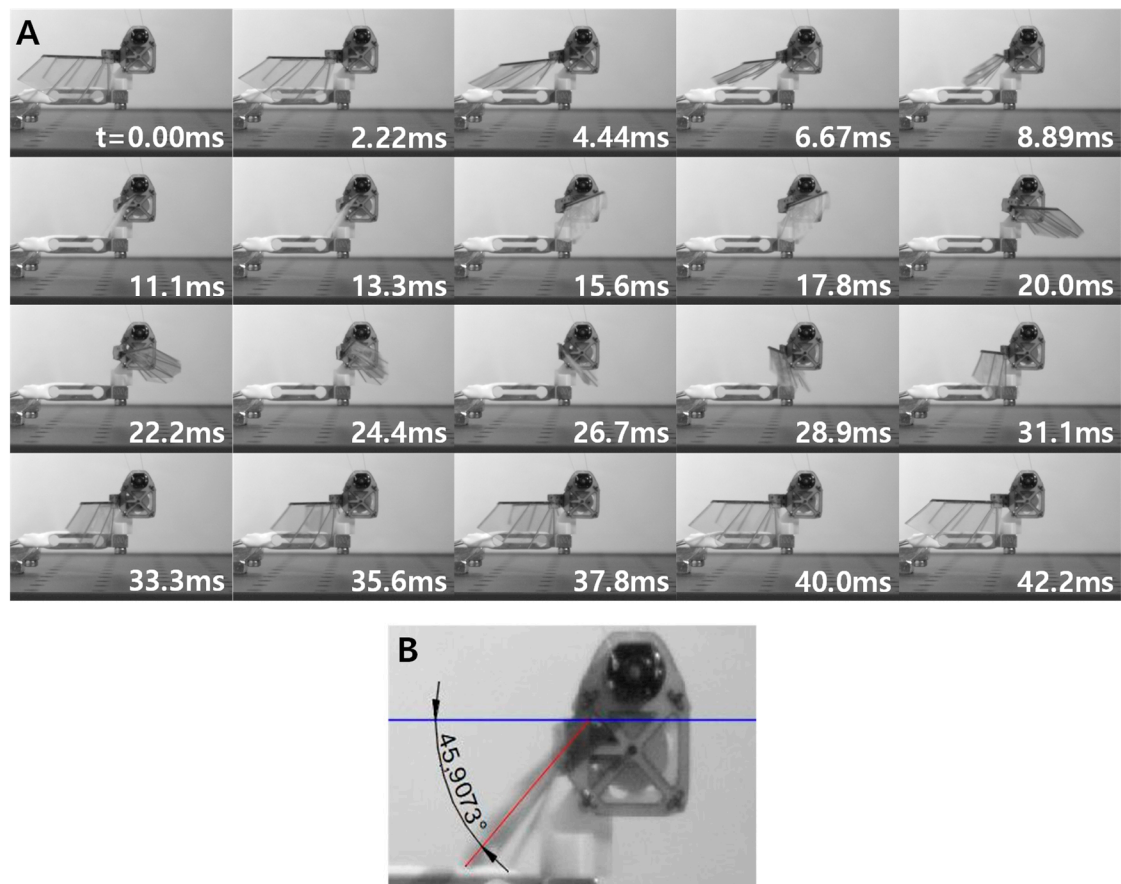


Figure 9. (A) Side view of the flapping mechanism at 23 Hz, taken at 900 fps. (B) Wing rotation angle can be measured.

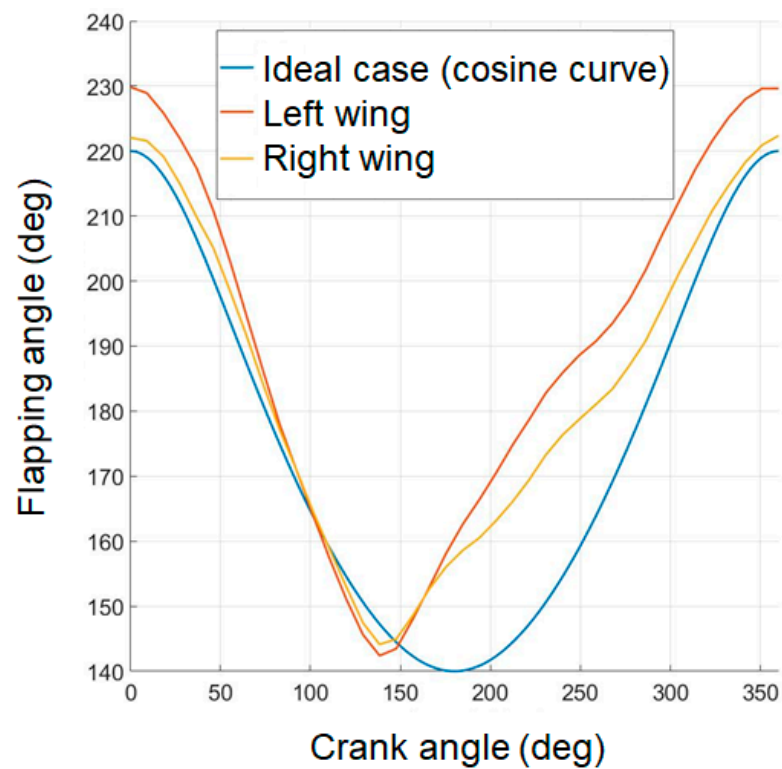
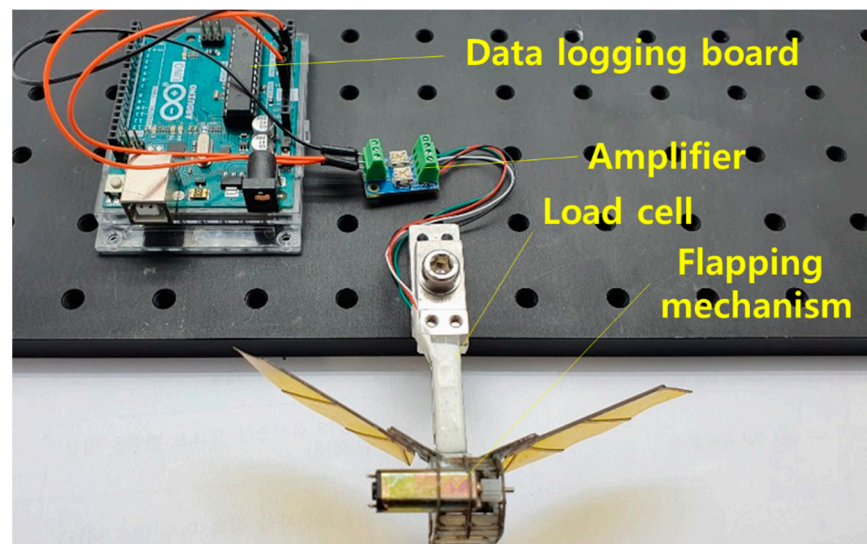


Figure 10. Comparison of flapping angle between the experimental case and the ideal case.

As previously said, in terms of overall trend, is it preferable that the relation between the flapping angle and the crank angle is close to the ideal cosine curve. However, Figure 10 shows the substantial difference between the experimental results and the ideal cosine curve. Especially for the upstroke, the gap between the experiment and the cosine curve tends to increase. In addition, the upstroke requires much time, compared to the downstroke. This can be explained by fabrication tolerance. This tolerance induces the flexures to make delay when they transmit the motion. During the upstroke, therefore, the motor's motion is transmitted with delay. However, in case of the downstroke, the facets structurally help to transmit the motor's motion and accordingly the delay does not occur.

#### 4.2. Thrust

To check whether the proposed transmission properly generates the thrust or not, force measurement has been done. The data are collected through a load cell shown in Figure 11, sampled with the rate of 1000 Hz and filtered with the cut-off frequency of 100 Hz. The filtered data and the averaged data are given in Figure 12. The average thrust is measured as 2.34 gf (=22.9 mN) at the flapping frequency of 23 Hz.



**Figure 11.** Experimental setup. A load cell has been used to measure the thrust. The signal goes to the amplifier and the amplified data are logged to the PC.

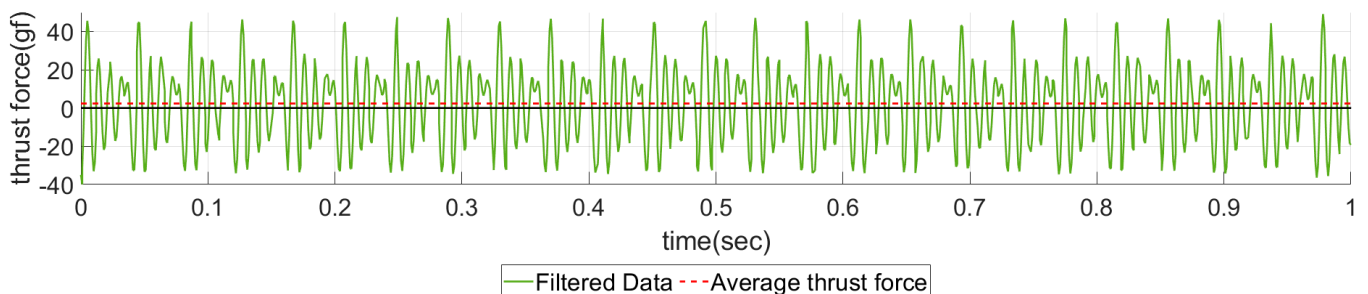


**Figure 12.** The measured thrust. The low-pass filtered data (solid line) and the average value (dashed line) are given.

The thrust is successfully generated since the wing rotation angle is observed as we intended, which is shown in Figure 11B. For the wing rotation, a passive hinge has been applied to get an additional degree of freedom. The stoppers, however, have been added to prevent the excessive wing rotation. As a result, an angle of attack (AoA) of about  $45^\circ$  has been observed as shown in Figure 11B. This AoA maintains during both the upstroke and downstroke. Consequently, the thrust can be generated.

## 5. Conclusions

In this paper, we proposed a novel transmission to reduce the assembly process and wear problems for DC motor-based FWMAVs. To make this possible, a geometrically constrained and origami-based spherical six-bar linkage has been suggested. The origami-based fabrication method reduces the relative moving parts such as pin joints and sliders, which resolves mechanical wear problems and assembly issues. The constrained spherical six-bar linkage passes only necessary motions by filtering the DC motor's rotating movement. Therefore, the linearly reciprocating movement is transferred and the flapping motion is successfully made. To demonstrate the feasibility of the proposed concept, flapping tests have been done to investigate the flapping angle, the wing rotation angle, and the vertical thrust. As a result, the suggested mechanism has shown a flapping angle of about  $80^\circ$ , a  $45^\circ$  wing rotation angle, 23 Hz of flapping frequency, and 2.34 gf (=22.9 mN) of the vertical thrust. Although the thrust is not enough to take off, we confirmed that the constrained spherical six-bar linkage successfully works as a transmission for the DC motor-based FWMAVs.

**Supplementary Materials:** The following are available online at <https://www.mdpi.com/2076-3417/11/4/1515/s1>, Video S1: Working process of the constrained spherical six-bar.

**Author Contributions:** Conceptualization, S.-Y.B. and G.-P.J.; methodology, S.-Y.B. and G.-P.J.; software, S.-Y.B.; validation, S.-Y.B. and G.-P.J.; formal analysis, S.-Y.B.; investigation, S.-Y.B.; resources, G.-P.J. and J.-S.K.; data curation, S.-Y.B.; writing—original draft preparation, S.-Y.B., J.-S.K. and G.-P.J.; writing—review and editing, J.-S.K. and G.-P.J.; visualization, S.-Y.B.; supervision, G.-P.J.; project administration, G.-P.J.; funding acquisition, G.-P.J. All authors have read and agreed to the published version of the manuscript.

**Funding:** This research was supported by a grant to Bio-Mimetic Robot Research Center Funded by Defense Acquisition Program Administration, and by Agency for Defense Development (UD190018ID). This research was also supported by Korea Institute for Advancement of Technology (KIAT) grant funded by the Korea Government (MOTIE) (P0008473, HRD Program for Industrial Innovation).

**Institutional Review Board Statement:** Not applicable.

**Informed Consent Statement:** Not applicable.

**Data Availability Statement:** Not applicable.

**Conflicts of Interest:** The authors declare no conflict of interest.

## References

1. Takahashi, H.; Abe, K.; Takahata, T.; Shimoyama, I. Experimental study of the aerodynamic interaction between the forewing and hindwing of a beetle-type ornithopter. *Aerospace* **2018**, *5*, 83. [[CrossRef](#)]
2. Karásek, M.; Muijres, F.T.; De Wagter, C.; Remes, B.D.; de Croon, G.C. A tailless aerial robotic flapper reveals that flies use torque coupling in rapid banked turns. *Science* **2018**, *361*, 1089–1094. [[CrossRef](#)] [[PubMed](#)]
3. Gong, D.; Lee, D.; Shin, S.J.; Kim, S. Design and Experiment of String-based Flapping Mechanism and Modulized Trailing Edge Control System for Insect-like FWMAV. In Proceedings of the 2018 AIAA Information Systems-AIAA Infotech@ Aerospace, Kissimmee, FL, USA, 8–12 January 2018; p. 0987.
4. De Wagter, C.; Karásek, M.; de Croon, G. Quad-thopter: Tailless flapping wing robot with four pairs of wings. *Int. J. Micro Air Veh.* **2018**, *10*, 244–253. [[CrossRef](#)]
5. Oppenheimer, M.W.; Sigthorsson, D.; Doman, D.B.; Weintraub, I. Wing design and testing for a tailless flapping wing micro-air vehicle. In Proceedings of the AIAA Guidance, Navigation, and Control Conference, Grapevine, TX, USA, 9–13 January 2017; p. 1271.
6. Yan, X.; Qi, M.; Lin, L. Self-lifting artificial insect wings via electrostatic flapping actuators. In Proceedings of the 2015 28th IEEE International Conference on Micro Electro Mechanical Systems (MEMS), Estoril, Portugal, 18–22 January 2015; pp. 22–25.
7. Hines, L.; Colmenares, D.; Sitti, M. Platform design and tethered flight of a motor-driven flapping-wing system. In Proceedings of the 2015 IEEE International Conference on Robotics and Automation (ICRA), Seattle, DC, USA, 26–30 May 2015; pp. 5838–5845.
8. Ristroph, L.; Childress, S. Stable hovering of a jellyfish-like flying machine. *J. R. Soc. Interface* **2014**, *11*, 20130992. [[CrossRef](#)] [[PubMed](#)]
9. Lau, G.-K.; Chin, Y.-W.; Goh, J.T.-W.; Wood, R.J. Dipteran-insect-inspired thoracic mechanism with nonlinear stiffness to save inertial power of flapping-wing flight. *IEEE Trans. Robot.* **2014**, *30*, 1187–1197. [[CrossRef](#)]

10. Hines, L.; Campolo, D.; Sitti, M. Liftoff of a motor-driven, flapping-wing microaerial vehicle capable of resonance. *IEEE Trans. Robot.* **2013**, *30*, 220–232. [[CrossRef](#)]
11. Gaissert, N.; Mugrauer, R.; Mugrauer, G.; Jebens, A.; Jebens, K.; Knubben, E.M. Inventing a micro aerial vehicle inspired by the mechanics of dragonfly flight. In Proceedings of the Conference Towards Autonomous Robotic Systems, London, UK, 3–5 July 2019; pp. 90–100.
12. Sahai, R.; Galloway, K.C.; Wood, R.J. Elastic Element Integration for Improved Flapping-Wing Micro Air Vehicle Performance. *IEEE Trans. Robot.* **2013**, *29*, 32–41. [[CrossRef](#)]
13. Keennon, M.; Klingebiel, K.; Won, H. Development of the nano hummingbird: A tailless flapping wing micro air vehicle. In Proceedings of the 50th AIAA Aerospace Sciences Meeting Including the New Horizons Forum and Aerospace Exposition, Nashville, TN, USA, 9–12 January 2012; p. 588.
14. Campolo, D.; Azhar, M.; Lau, G.-K.; Sitti, M. Can DC motors directly drive flapping wings at high frequency and large wing strokes? *IEEE/ASME Trans. Mechatron.* **2012**, *19*, 109–120. [[CrossRef](#)]
15. Galiński, C.; Żbikowski, R. Insect-like flapping wing mechanism based on a double spherical Scotch yoke. *J. R. Soc. Interface* **2005**, *2*, 223–235. [[CrossRef](#)]
16. Roshanbin, A.; Altartouri, H.; Karasek, M.; Preumont, A. COLIBRI: A hovering flapping twin-wing robot. *Int. J. Micro Air Veh.* **2017**, *9*, 270–282. [[CrossRef](#)]
17. Phan, H.V.; Au, T.K.L.; Park, H.C. Clap-and-fling mechanism in a hovering insect-like two-winged flapping-wing micro air vehicle. *R. Soc. Open Sci.* **2016**, *3*, 160746. [[CrossRef](#)]
18. Phan, H.V.; Truong, Q.T.; Au, T.K.L.; Park, H.C. Optimal flapping wing for maximum vertical aerodynamic force in hover: Twisted or flat? *Bioinspiration Biomim.* **2016**, *11*, 046007. [[CrossRef](#)] [[PubMed](#)]
19. Phan, H.V.; Kang, T.; Park, H.C. Design and stable flight of a 21 g insect-like tailless flapping wing micro air vehicle with angular rates feedback control. *Bioinspiration Biomim.* **2017**, *12*, 036006. [[CrossRef](#)]
20. Wood, R.J. The First Takeoff of a Biologically Inspired At-Scale Robotic Insect. *IEEE Trans. Robot.* **2008**, *24*, 341–347. [[CrossRef](#)]
21. Fuller, S.B. Four wings: An insect-sized aerial robot with steering ability and payload capacity for autonomy. *IEEE Robot. Autom. Lett.* **2019**, *4*, 570–577. [[CrossRef](#)]
22. Arabagi, V.; Hines, L.; Sitti, M. Design and manufacturing of a controllable miniature flapping wing robotic platform. *Int. J. Robot. Res.* **2012**, *31*, 785–800. [[CrossRef](#)]
23. Steltz, E.; Wood, R.J.; Avadhanula, S.; Fearing, R.S. Characterization of the micromechanical flying insect by optical position sensing. In Proceedings of the 2005 IEEE International Conference on Robotics and Automation, Barcelona, Spain, 18–22 April 2005; pp. 1252–1257.
24. Roll, J.A.; Cheng, B.; Deng, X. Design, fabrication, and experiments of an electromagnetic actuator for flapping wing micro air vehicles. In Proceedings of the 2013 IEEE International Conference on Robotics and Automation, Karlsruhe, Germany, 6–10 May 2013; pp. 809–815.
25. Roll, J.A.; Cheng, B.; Deng, X. An electromagnetic actuator for high-frequency flapping-wing microair vehicles. *IEEE Trans. Robot.* **2015**, *31*, 400–414. [[CrossRef](#)]
26. Bontemps, A.; Vanneste, T.; Paquet, J.; Dietsch, T.; Grondel, S.; Cattan, E. Design and performance of an insect-inspired nano air vehicle. *Smart Mater. Struct.* **2012**, *22*, 014008. [[CrossRef](#)]
27. Meng, K.; Zhang, W.; Chen, W.; Li, H.; Chi, P.; Zou, C.; Wu, X.; Cui, F.; Liu, W.; Chen, J. The design and micromachining of an electromagnetic MEMS flapping-wing micro air vehicle. *Microsyst. Technol.* **2012**, *18*, 127–136. [[CrossRef](#)]
28. Zou, Y.; Zhang, W.; Zhang, Z. Liftoff of an electromagnetically driven insect-inspired flapping-wing robot. *IEEE Trans. Robot.* **2016**, *32*, 1285–1289. [[CrossRef](#)]
29. Suzuki, K.; Shimoyama, I.; Miura, H. Insect-model based microrobot with elastic hinges. *J. Microelectromech. Syst.* **1994**, *3*, 4–9. [[CrossRef](#)]
30. Wood, R.J.; Avadhanula, S.; Sahai, R.; Steltz, E.; Fearing, R.S. Microrobot design using fiber reinforced composites. *J. Mech. Des.* **2008**, *130*, 052304. [[CrossRef](#)]
31. Koh, J.-S.; Cho, K.-J. Omega-Shaped Inchworm-Inspired Crawling Robot with Large-Index-and-Pitch (LIP) SMA Spring Actuators. *IEEE/ASME Trans. Mechatron.* **2013**, *18*, 419–429. [[CrossRef](#)]
32. Nguyen, Q.V.; Park, H.C.; Goo, N.S.; Byun, D. Characteristics of a Beetle’s Free Flight and a Flapping-Wing System that Mimics Beetle Flight. *J. Bionic Eng.* **2010**, *7*, 77–86. [[CrossRef](#)]
33. Nguyen, Q.V.; Truong, Q.T.; Park, H.C.; Goo, N.S.; Byun, D. A motor-driven flapping-wing system mimicking beetle flight. In Proceedings of the 2009 IEEE International Conference on Robotics and Biomimetics (ROBIO), Bangkok, Thailand, 22–25 February 2009; pp. 1087–1092.
34. Steltz, E.; Avadhanula, S.; Fearing, R.S. High lift force with 275 Hz wing beat in MFL. In Proceedings of the 2007 IEEE/RSJ International Conference on Intelligent Robots and Systems, San Diego, CA, USA, 29 October–2 November 2007; pp. 3987–3992.